Calculation of the Be-Ni Phase Diagram

Anirudh Bali,

The Department of Mechanical and Materials Engineering,

University of Cincinnati,

Cincinnati, OH

12/08/2025

Abstract

The purpose of this study is to establish a publicly available thermodynamic database for the beryllium-nickel system – a system whose thermodynamic database is currently unavailable publicly. The study begins with the calculation of thermodynamic properties for pure Ni and Be, leading to the calculation of unary phase diagrams for both elements. To calculate the binary system's thermodynamic database, experimental thermodynamic data was used alongside the ESPEI Python library to calculate thermodynamic model parameters using the CALPHAD methodology. These parameters were encoded into a .tdb file which was then plotted using the ESPEI library and Pandat to assess accuracy of the generated .tdb file against an authoritative Be-Ni phase diagram. This study's phase diagram successfully estimated features of the Be-Ni phase diagram such as component phase transition temperatures and phase boundary topology. Inaccuracies in estimated phase field geometries, invariant reactions, and melting temperatures highlight the need to optimize thermodynamic model parameters using zero-point function experimental data to produce an accurate Be-Ni thermodynamic database.

Keywords: Phase diagram, Beryllium, Nickel, Be-Ni, CALPHAD, ESPEI

1. Introduction

The calculation of phase diagrams is central to the practice of materials thermodynamics. This study attempts to calculate the binary phase diagram for the beryllium-nickel (Be-Ni) system. Although a calculated phase diagram has been established for the Be-Ni system as early as 1988

by Okamoto and Tanner [1], a publicly available thermodynamic dataset (.tdb) for this system has yet to be published. This limits the scientific community's ability to further investigate this binary alloy system and investigate ternary systems that include the Be-Ni system.

2. Methods

This study calculates the binary phase diagram for the Be-Ni system using the CALPHAD technique. The following section outlines the thermodynamic principles and numerical techniques utilized to calculate the binary phase diagram of interest, beginning with an investigation into the thermodynamic properties of the pure elements in the system. NIST-JANAF was the primary source used for temperature-dependent specific heat capacity data of pure Ni [3] and pure Be [4]. Table 1 summarizes select material properties reported by NIST-JANAF that will be utilized to define polynomial functions for specific heat capacity, enthalpy, and entropy with respect to temperature for each pure element.

Table 1. NIST-JANAF data for Ni [3] and Be [4]

Standard State Pressure ($P°$)	0.1 MPa
Enthalpy Reference Temperature (T_r)	298.15 K
Nickel (Ni)	
C_p Lambda Maximum Transition Temp. (T_λ)	631.000 K
Melting Temperature (T_m)	1728.000 K
Vaporization Temperature (T_v)	3156.584 K
Beryllium (Be)	
αBe -βBe Transition Temp. (T_α)	1527.000 K
Melting Temperature (T_m)	1560.000 K
Vaporization Temperature (T_v)	2741.437 K

2.1 Deriving Standard State Enthalpy and Entropy Functions

Equation 1, the Shomate equation, is the polynomial expression used to curve fit specific heat capacity data to define $C_p(T)$ for Ni and Be from 0 K to 6000 K. Across this temperature range,

both Ni and Be undergo three phase transformations: (1) a solid-to-solid, (2) a solid-to-liquid, and (3) a liquid-to-gas transformation, occurring at their respective temperatures as reported in Table 1. The discontinuities in specific heat capacity data at phase transformations necessitate that $C_p(T)$ be defined as a piecewise function.

$$C_p(T) = a + bT + cT^2 + dT^3 + \frac{e}{T^2} \tag{1}$$

To calculate the polynomial coefficients for each phase, MATLAB's fittype and fit function were used. The fittype function defined the form of the fitted polynomial and the fit function calculated the unknown coefficients [5, 6]. Equation 1 is the full form of the Shomate equation; however, not all terms are strictly necessary to achieve good fits to NIST-JANAF data. For both Ni and Be, higher order terms of the Shomate equation were excluded as needed for different intervals of the piecewise specific heat function to achieve the most agreeable fit. Refer to the results reported in Table X for the exact form of the Shomate equation used for Ni and Be across their respective piecewise intervals.

$$H(T) = \int C_p \, dT \tag{2}$$

$$S(T) = \int \frac{C_p}{T} \, dT \tag{3}$$

Equation 2 and Equation 3 were used to derive expressions for enthalpy and entropy as a function of temperature, $H(T)$ and $S(T)$ respectively. Equation 4 and Equation 5 are the general forms of $H(T)$ and $S(T)$ derived from integrating Equation 1, the full form of the Shomate equation. Recognize that the coefficients a through e are the coefficients evaluated when curve-fitting $C_p(T)$ from 0 K to 6000 K and vary with phase.

$$H(T) - H(T_0) = aT + \frac{bT^2}{2} + \frac{cT^3}{3} + \frac{dT^4}{4} - \frac{e}{T} + f \tag{4}$$

$$S(T) - S(T_0) = a \ln T + bT + \frac{cT^2}{2} + \frac{dT^3}{3} - \frac{e}{2T^2} + g \quad (5)$$

Due to the piecewise nature of $C_p(T)$, the unknown integration constants, f and g, vary for each phase. To evaluate the value of f and g for each phase, the $C_p(T)$ Shomate polynomials can be integrated using MATLAB's integral function, according to Equation 2 and Equation 3, to establish initial values, $H(T_0)$ and $S(T_0)$, for each phase. This operation is not required for $H(T)$ and $S(T)$ from 0 K to $T_{\lambda/\alpha}$ because the standard enthalpy, $H°(T_r)$, and standard entropy, $S°(100\ K)$, from the NIST-JANAF database can be used instead, Table 3.

For Ni, MATLAB's integral function was unable to numerically integrate Equation 5 from 0 K to 100 K; therefore, Ni's entropy is defined starting at 100 K rather than 0 K. This simplification is acceptable for the purposes of subsequent phase diagram calculations as entropy data from 0 K to 100 K is not critical to calculating the unary phase diagrams of Be and Ni and outside the temperature of interest for the binary Be-Ni phase diagram. For consistency between the two pure elements, the entropy of Be is also defined from 100 K rather than 0 K.

Table 3. NIST-JANAF data used in enthalpy and entropy calculations [3], [4]

Nickel	
$H°(T_r)$	0. kJ mol^{-1}
$S°(100\ K)$	7.454 J K^{-1} mol^{-1}
Beryllium	
$H°(T_r)$	0. kJ mol^{-1}
$S°(100\ K)$	0.503 J K^{-1} mol^{-1}

2.2 Defining Gibbs Free Energy Functions

The calculation of a pure element's unary phase diagram amounts to identifying the equilibrium phase for a given system state. Thermodynamically, this is equivalent to identifying the phase with the lowest Gibbs free energy for the system state in question. To do this, the Gibbs

free energy of each phase must be defined for the entire temperature range being considered. Therefore, $H(T)$ and $S(T)$ for each phase needs to be defined for the entire temperature range being considered, as they are necessary to calculate Gibbs free energy, Equation 6.

$$G(T) = H(T) - TS(T) \tag{6}$$

Equations 7-12 define $H(T)$ and $S(T)$ from 0 to 6000 K for the solid, liquid, and gas phases of Ni and Be. Each phase has different coefficients which are assumed to be constant from 0 to 6000 K; therefore, Equations 7-12 are simply the enthalpy and entropy functions already calculated for each phase extrapolated across the entire temperature range of interest. For the solid phase, higher order terms of the Shomate equation were excluded due to unrealistic behavior ($H_{solid}(T) < H_{liquid}(T)$ and $\frac{dH_{solid}}{dT} < 0$) as the function was extrapolated from 0 to 6000 K. Assuming a constant specific heat, $C_{p,solid}(T) = a$, for the solid phase led to a more well-behaved $H_{solid}(T)$ in the case of Ni and Be. Secondly, identifying differences between the solid phases of each pure element was not of significant interest; therefore, the higher temperature solid phase was selected to define $H_{solid}(T)$ and $S_{solid}(T)$ for Ni and Be.

$$H_{solid}(T) = aT + f_{solid} \tag{7}$$

$$H_{liquid}(T) = aT + \frac{bT^2}{2} + \frac{cT^3}{3} + \frac{dT^4}{4} - \frac{e}{T} + f_{liquid} \tag{8}$$

$$H_{gas}(T) = aT + \frac{bT^2}{2} + \frac{cT^3}{3} + \frac{dT^4}{4} - \frac{e}{T} + f_{gas} \tag{9}$$

$$S_{solid}(T) = a\ln T + g_{solid} \tag{10}$$

$$S_{liquid}(T) = a\ln T + bT + \frac{cT^2}{2} + \frac{dT^3}{3} - \frac{e}{2T^2} + g_{liquid} \tag{11}$$

$$S_{gas}(T) = a\ln T + bT + \frac{cT^2}{2} + \frac{dT^3}{3} - \frac{e}{2T^2} + g_{gas} \tag{12}$$

Using enthalpy and entropy functions defined for each phase, the Gibbs free energy as a function of temperature and pressure can be defined for solid, liquid, and gas phases, Equations 13-15. The additional term in Equations 13-15 compared to Equation 6 is a pressure correction term included to account for the pressure dependence of Gibbs free energy [7]. This term is particularly important to include for the gas phase, where pressure dependence is significant.

$$G_{solid}(T,P) = H°_{solid}(T) - TS°_{solid}(T) + V_m(P - P°) \quad (13)$$

$$G_{liquid}(T,P) = H°_{liquid}(T) - TS°_{liquid}(T) + V_m(P - P°) \quad (14)$$

$$G_{gas}(T,P) = H°_{gas}(T) - TS°_{gas}(T) + RT\ln\left(\frac{P}{P°}\right) \quad (15)$$

Using equations 13-15, the Gibbs free energy of the solid, liquid, and gas phase of a pure element can be calculated for pressures and temperature values across intervals of interest. The phase with the lowest Gibbs energy is the equilibrium phase, and the state of matter the pure element takes on, for the evaluated pressure-temperature condition. It is important to note that this formulation of Gibbs free energy treats the gas phases of Ni and Be as ideal gases.

2.3 Calculation of Triple Point

At the triple point, where solid, liquid, and gas phases coexist at equilibrium, Equation 16 must be satisfied.

$$G_{solid}(T,P) = G_{liquid}(T,P) = G_{gas}(T,P) \quad (16)$$

If Equation 16 is not satisfied, it implies there is at least one phase that has a lower energy state than the others, making it the thermodynamically favored phase of the material so the three phases will not coexist. To find the specific temperature and pressure where all three phases can coexist, the conditions where the Gibbs free energies of all three phases are equal must be solved for. This equates to solving for the values of T and P that satisfy Equation 16, which can be expressed as two independent constraint equations, Equation 17 and Equation 18.

$$g(T,P) = G_{solid}(T,P) - G_{liquid}(T,P)\,, \qquad g(T,P) = 0 \tag{17}$$

$$h(T,P) = G_{solid}(T,P) - G_{gas}(T,P), \qquad h(T,P) = 0 \tag{18}$$

Equation 17 and Equation 18 are used to define the Lagrangian function, Equation 19, which sets ups a constrained optimization problem that can be solved to identify the triple point,

$$\mathcal{L}(T,P,\lambda,\mu) = f(T,P) + \lambda g(T,P) + \mu h(T,P) \tag{19}$$

where $f(T,P)$ is the objective function, $g(T,P)$ and $h(T,P)$ are constraint functions, and λ and μ are Lagrange multipliers. Recognize, with this setup, an arbitrary objective function can be defined as the two constraint functions are sufficient to define the system of equations needed to solve for the four unknowns $T, P, \lambda,$ and μ (two constraint functions, each with two partial derivatives). Therefore, calculations in MATLAB were carried out using $f(T,P) = 0$ for simplicity. By solving this system of equations, what is being calculated is the combination of temperature and pressure that satisfy Equation 16.

To solve the system of equations for T and P, MATLAB's fmincon function was used. This function is specifically designed to find the minimum of constrained nonlinear multivariable functions numerically [8]. In this case, since $f(T,P) = 0$, fmincon is not solving for a true minimum, rather it is simply solving for the conditions that satisfy the two constraint equations (which is a root-finding problem).

2.4 Calculation of Unary Phase Diagrams

In addition to calculating the triple point, the Gibbs free energy functions of the solid, liquid, and gas phase of Ni and Be were used to calculate the field-field and field-density phase diagrams for each pure element. Of particular interest is how the triple point on a field-field diagram transforms into a horizontal tie-line on a field-density diagram.

The field-field (pressure-temperature) phase diagram was the first to be calculated. MATLAB was used to evaluate Equations 13-15 from 0 K to 6000 K and 1 Pa to 10^{10} Pa to identify the equilibrium phase using the comparison procedure described in Section 2.2. After evaluating the state of matter at each combination of temperature and pressure within this P-T search space, the pressure-temperature phase diagram for each pure element can be produced to visualize the phase fields of each pure element, two-phase coexistence curves, and the element's triple point. Calculation of the field-field phase diagram in this way makes it straightforward to numerically evaluate the "location" of the two-phase coexistence curves in P-T space and validate the calculated triple point. Identifying the two-phase coexistence curves is necessary, as translating these coexistence curves from one domain to another is the key to evaluating field-density phase diagrams. For each pressure-temperature combination, the differences $G_{solid}(T,P) - G_{liquid}(T,P)$, $G_{liquid}(T,P) - G_{gas}(T,P)$, and $G_{solid}(T,P) - G_{gas}(T,P)$ where calculated. If these differences were within a relative tolerance of 0.00025, 0.001, and 0.001 J mol^{-1} respectively, that point was considered to be on the solid-liquid, liquid-gas, or solid-gas two-phase coexistence curve. The relative tolerance for each coexistence curve was tuned manually to achieve the minimum number of data points for smooth coexistence curves.

For each two-phase coexistence curve (solid-liquid, liquid-gas, and solid-gas) in P-T space, each point along these curves is a fixed thermodynamic state, fully defined by temperature and pressure. To transform these field-field phase boundaries into field-density phase boundaries in P-S space, S_m can be calculated using Equations 10-12 for the two phases on each coexistence curve. Therefore, one phase boundary in P-T space results in two phase boundaries in P-S space (one for each phase on the P-T phase boundary). Tie-lines connecting the initial and final points of the two P-S curves calculated for each P-T coexistence curve establish the two-phase areas in PS-space.

2.5 Calculation of Binary Thermodynamic Database and Phase Diagram

The ultimate aim of this study is to generate a thermodynamic database for Be-Ni, a binary system not published in the SGTE collection of publicly available binary datasets. The development of a thermodynamic database (also referred to as a .tdb file) involves three principal components: (1) collection and formatting of experimental thermodynamic data, (2) defining the thermodynamic models used to represent the Gibbs energy of each possible phase in the alloy system, and (3) optimization of model parameters to fit experimental observations.

The .tdb file is essential to calculating binary phase diagrams as the models defined within the .tdb file establish the Gibbs energy of each phase as a function of temperature and composition. Therefore, similar to the procedure described in Section 2.2 and applied to the calculation of unary phase diagrams, the binary phase diagram can be calculated using the thermodynamic principle of minimizing the Gibbs energy of the system.

This section provides an overview of the procedure followed to generate an initial thermodynamic database for the Be-Ni system. The database generated is used to calculate a Be-Ni phase diagram which will be compared to the established Be-Ni phase diagram to assess the viability of the procedure followed to construct the .tdb file.

2.5.1 Collection, Formatting, and Use of Experimental Thermodynamic Data

Okamoto and Tanner's assessment of the Be-Ni phase diagram [1] was the primary source for experimental thermodynamic data as it has been accepted, as recently as 2016 in the ASM Handbook of Alloy Phase Diagrams, as an authoritative source on the Be-Ni system. The following data published by Okamoto was used to calculate thermodynamic database for the Be-Ni system:

1. Be-Ni crystal structure data
2. Enthalpy of mixing for αBe, βBe, and Ni
3. Enthalpy of formation for β (BeNi) and γ ($Be_{21}Ni_5$)

This data was formatted into .json files using the ESPEI (Extensible Self-optimizing Phase Equilibria Infrastructure) phase models and dataset schema for subsequent CALPHAD model calculations [9], [10].

Once the system's phases and enthalpy of mixing/formation experimental data was formatted for the ESPEI library, the library's built-in functions were used to generate an initial fit for thermodynamic model parameters. Readers interested in details of how these parameters are calculated may reference an example published by ESPEI [11].

3. Results

Figure 1 and Figure 2 are, respectively, plots of Ni and Be's specific heat capacity as a function of temperature. NIST-JANAF data points are plotted alongside the curve fit Shomate equations used to estimate the specific heat capacity function used in subsequent calculations for $H(T)$ and $S(T)$. As mentioned, two different forms of the Shomate equation were used depending on the temperature range the function was being evaluated for. From 0 K to T_λ for Ni and 0 K to T_α for Be, corresponding to the red curves in Figure 1 and Figure 2, Equation 1 was used due to the highly nonlinear nature of Ni and Be's heat capacity. For $T > T_{\lambda/\alpha}$, Equation 2 was used. As highlighted in the graph, the Shomate equations were curve-fit in a piecewise manner to accommodate the discontinuities in specific heat associated with phase transformations. This is represented visually by the different colored lines plotted for each figure, each corresponding to one temperature range within that piecewise function. Table 4 reports the calculated Shomate coefficients for each pure element.

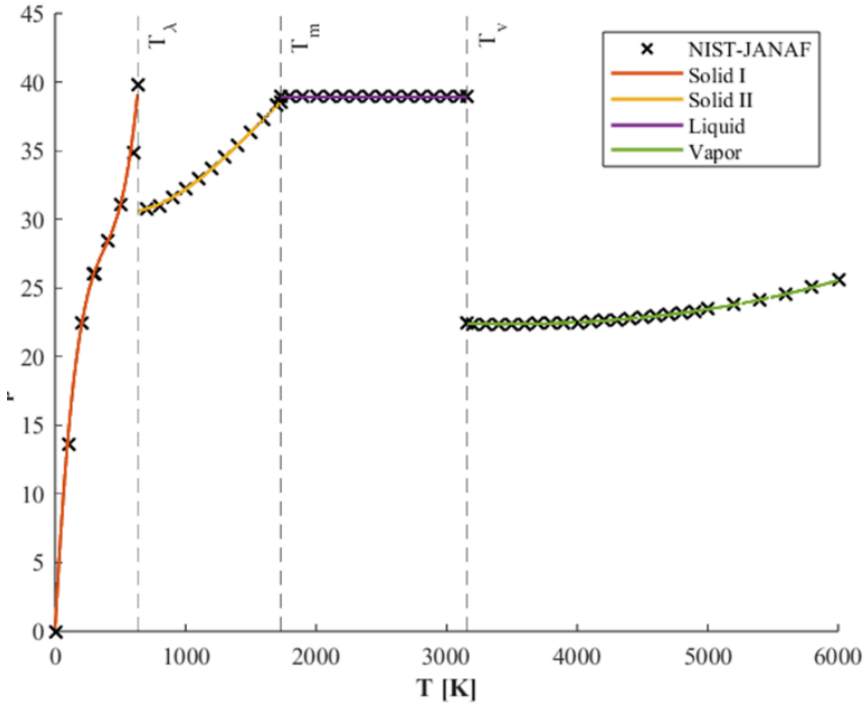

Figure 1. Specific Heat Capacity vs Temperature, Ni

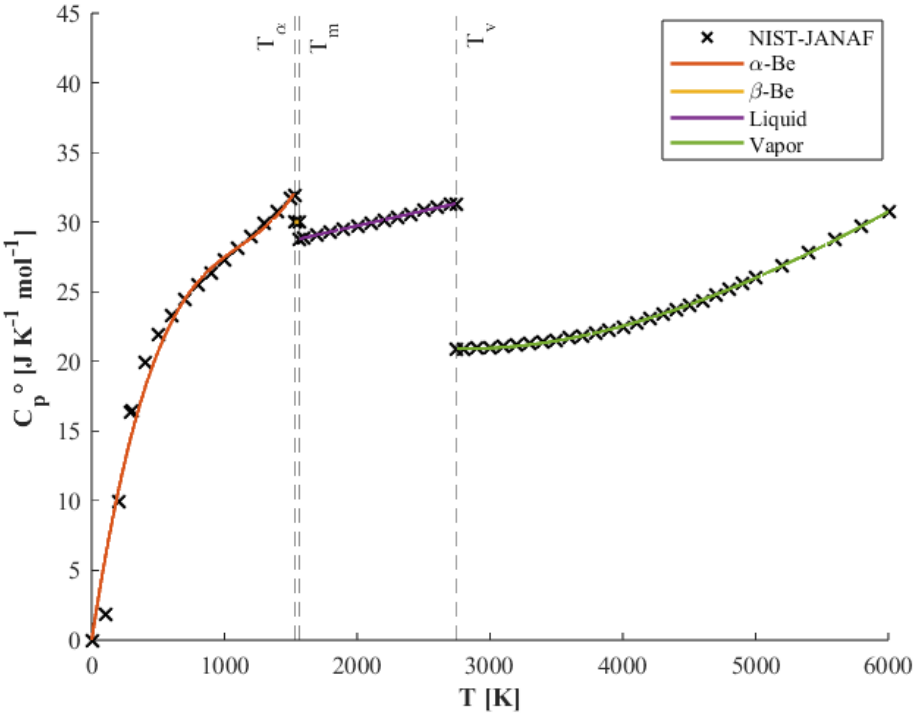

Figure 2. Specific Heat Capacity vs Temperature, Be

Table 4. Calculated Shomate equation polynomial coefficients (for equations in J mol^{-1})

T [K]	a	b	c	d	e
Nickel					
0 – 631	0.1884	0.1795	– 4.2182 e–04	3.7262 e–07	-
631 – 1728	33.4004	– 0.0116	1.3094 e–05	– 2.6924 e–09	2.6588 e–04
1728 – 3156.584	38.9110	0	0	0	0
3156.584 – 6000	24.8091	– 9.0041 e–04	– 9.9479 e–08	4.5047 e–11	0
Beryllium					
0 – 1527	0	0.0629	– 5.0678 e–05	1.5211 e–08	-
1527 – 1560	30	0	-	-	-
1560 – 2741.437	25.4360	0.0021	1.2553 e–09	– 1.8976 e–13	– 3.7842 e–05
2741.437 – 6000	33.0403	-0.0094	2.0591 e–06	– 9.3778 e–11	-3.9988 e–32

Figure 3 and Figure 4 are plots of enthalpy as a function of temperature for Ni and Be, respectively. Like specific heat, NIST-JANAF data points are plotted alongside the calculated curves for reference. Note that Equation 3 was used to calculate the enthalpy function for each phase. These curves are not functions calculated through regression of known data points like specific heat capacity. Figure 5 and Figure 6 are plots of entropy as a function of temperature and were calculated using Equation 4. For Figure 1-6, the calculated results show strong agreement with the NIST-JANAF dataset values.

Figure 7 and Figure 8 illustrate plots of Equation 8-10 and Equation 11-13 for Ni and Be, respectively. These equations are plotted alongside NIST-JANAF enthalpy and entropy data for reference. Table 5 reports on the integration constants calculated for Equations 8-13.

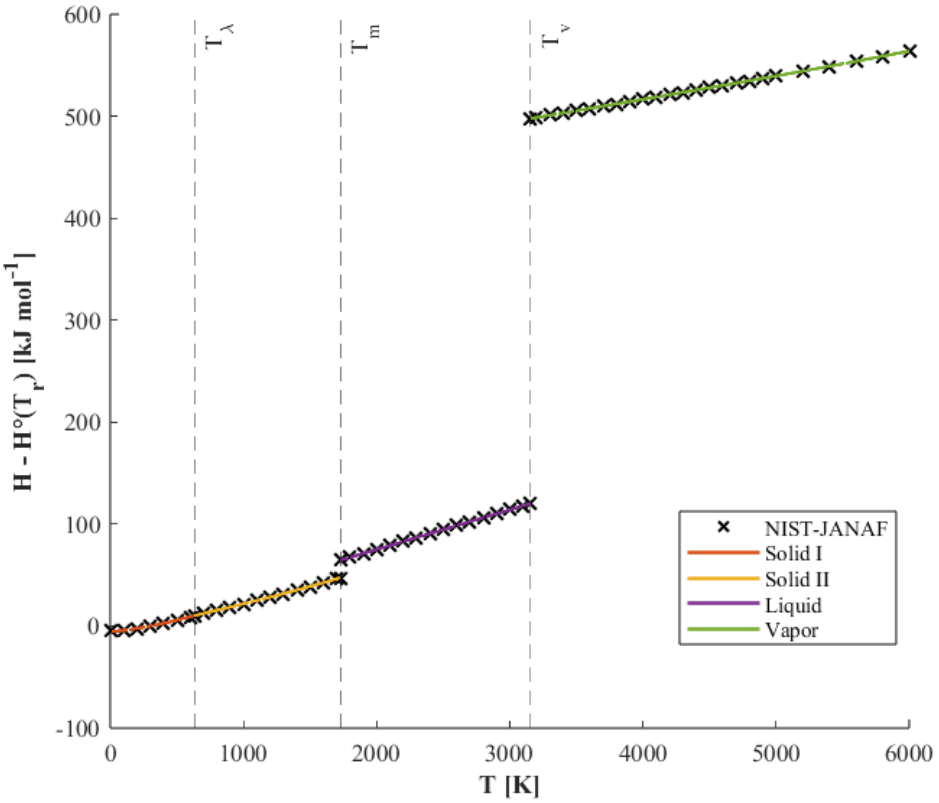

Figure 3. Enthalpy vs Temperature, Ni

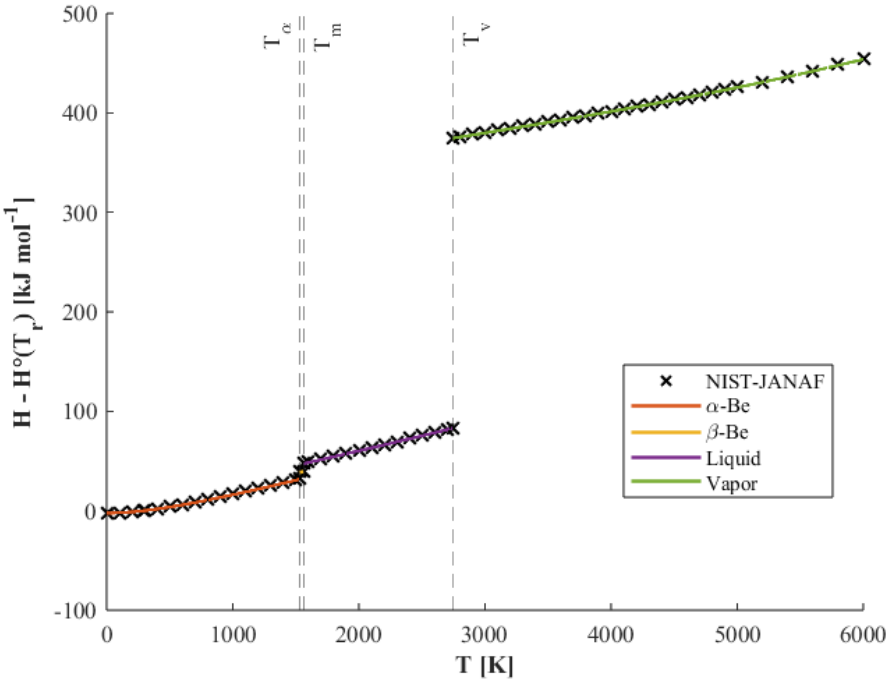

Figure 4. Enthalpy vs Temperature, Be

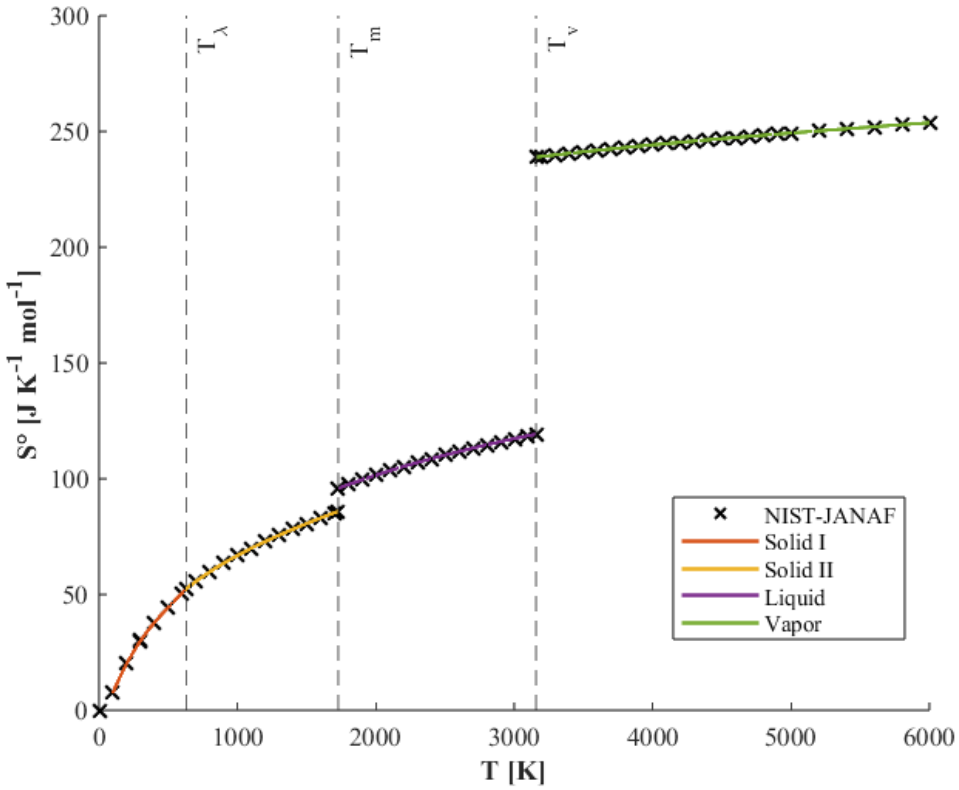

Figure 5. Entropy vs Temperature, Ni

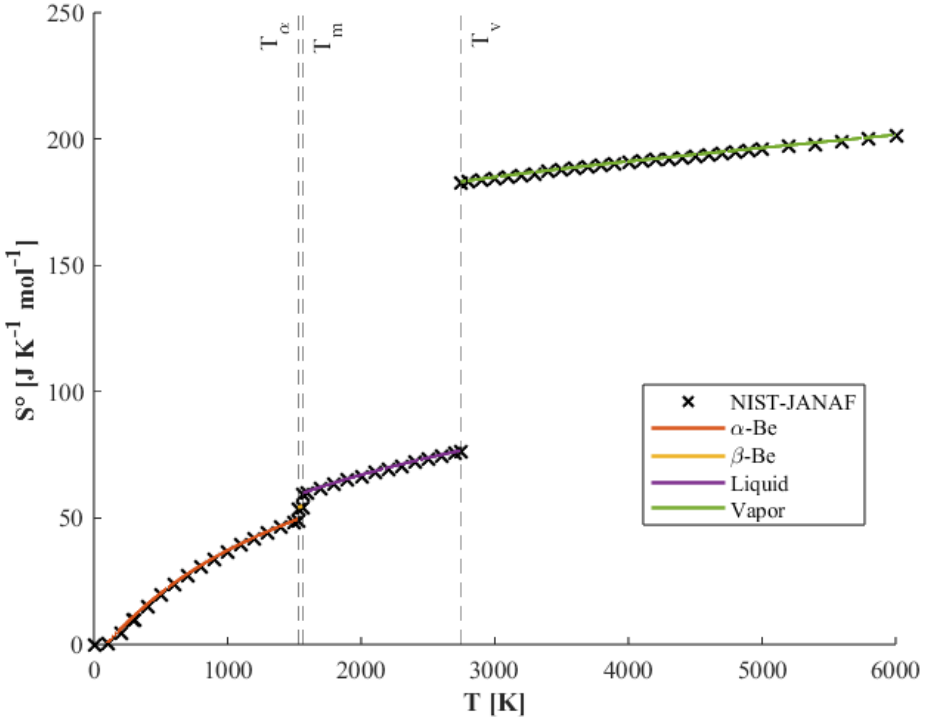

Figure 6. Entropy vs Temperature, Be

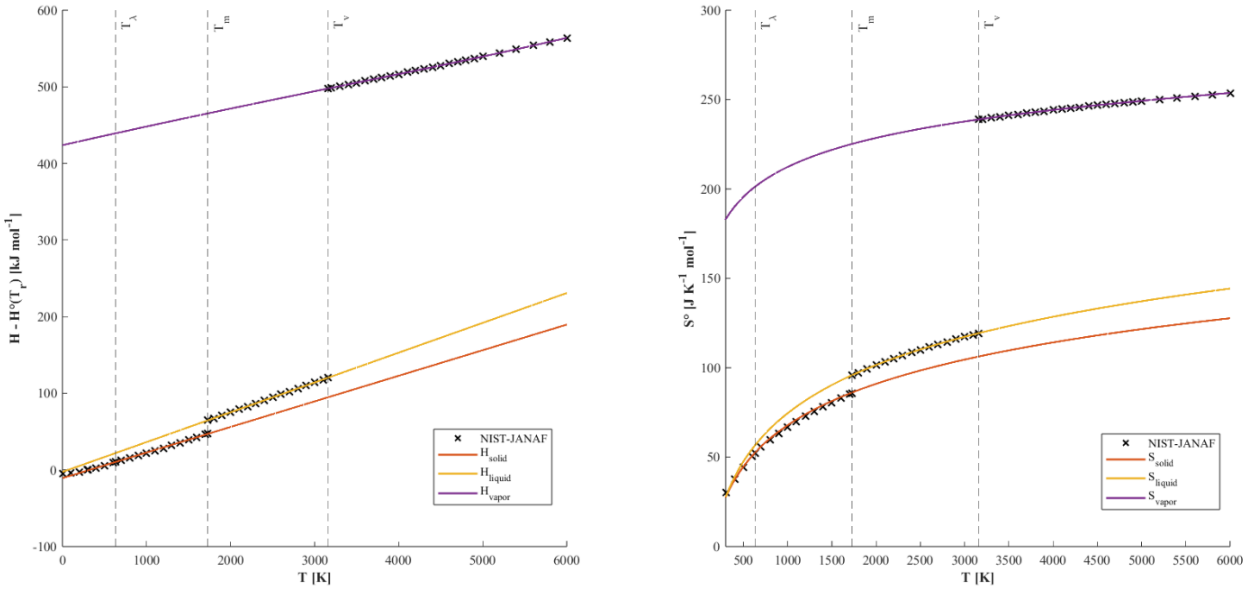

Figure 7. Extrapolated $H_{solid}, H_{liquid}, H_{vapor}$ (left) and extrapolated $S_{solid}, S_{liquid}, S_{vapor}$ (right), Ni

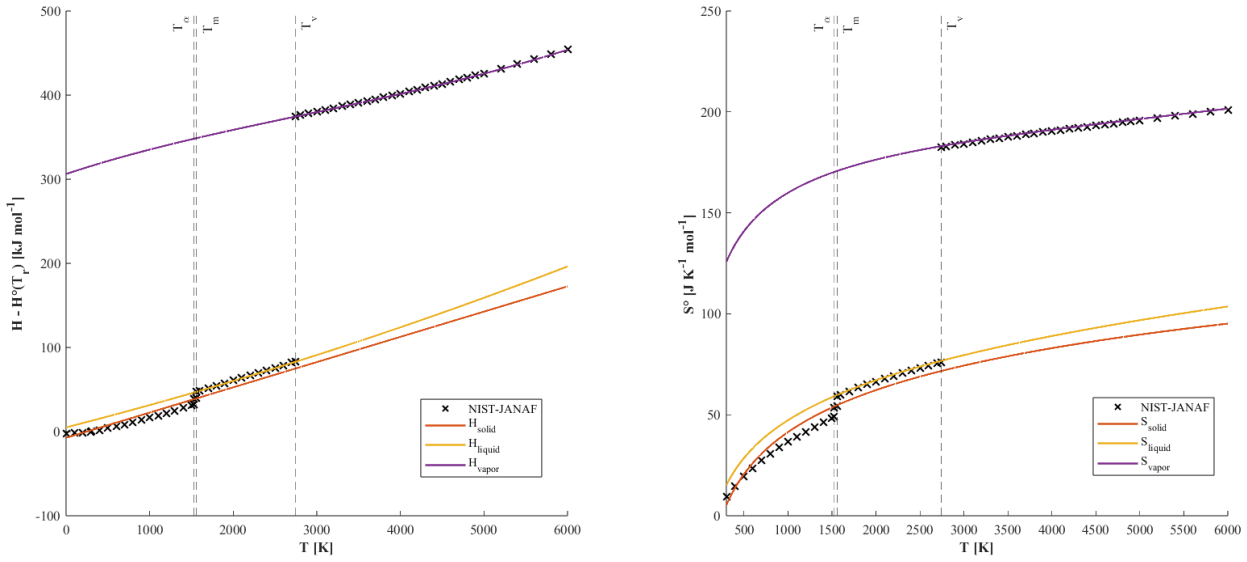

Figure 8. Extrapolated $H_{solid}, H_{liquid}, H_{vapor}$ (left) and extrapolated $S_{solid}, S_{liquid}, S_{vapor}$ (right), Be

Table 5. Calculated integration constants for Equation 8-13 (in kJ mol^{-1} and J mol^{-1} K^{-1} respectively)

f_{solid}	f_{liquid}	f_{gas}	g_{solid}	g_{liquid}	g_{gas}
Nickel					
– 10.823	– 2.6941	423.78	– 162.8893	–194.2502	41.8453
Beryllium					
– 7.4256	4.9751	306.14	-165.8465	-130.5802	-59.9601

Table 6 reports the calculated triple point of Ni and Be by solving the system of equations derived from Equations 18-20 using MATLAB's fmincon function. The function met the default stopping criteria and converged after the sixth iteration for both Ni and Be.

Table 6. Calculated triple points

Nickel	
T_t	1814.8 K
P_t	1.6685 Pa
Beryllium	
T_t	1560 K
P_t	5.0241 Pa

Figure 9 and Figure 10 present a visualization of the triple point calculation by simultaneously plotting the Gibbs free energy of the solid, liquid, and gas phase for each pure element at standard state pressure (1 atm) and the triple point pressure. These figures provide a graphical visualization of what MATLAB's fmincon function is solving for using numerical techniques.

Figure 11 and Figure 12 illustrate the calculated field-field phase diagram (pressure-temperature) for pure Ni and pure Be, respectively. Each single-phase region is uniquely colored, and the triple point reported in Table 6 is plotted as a red dot. Figure 13 and Figure 14 illustrate the calculated field-density phase diagram (pressure-molar entropy).

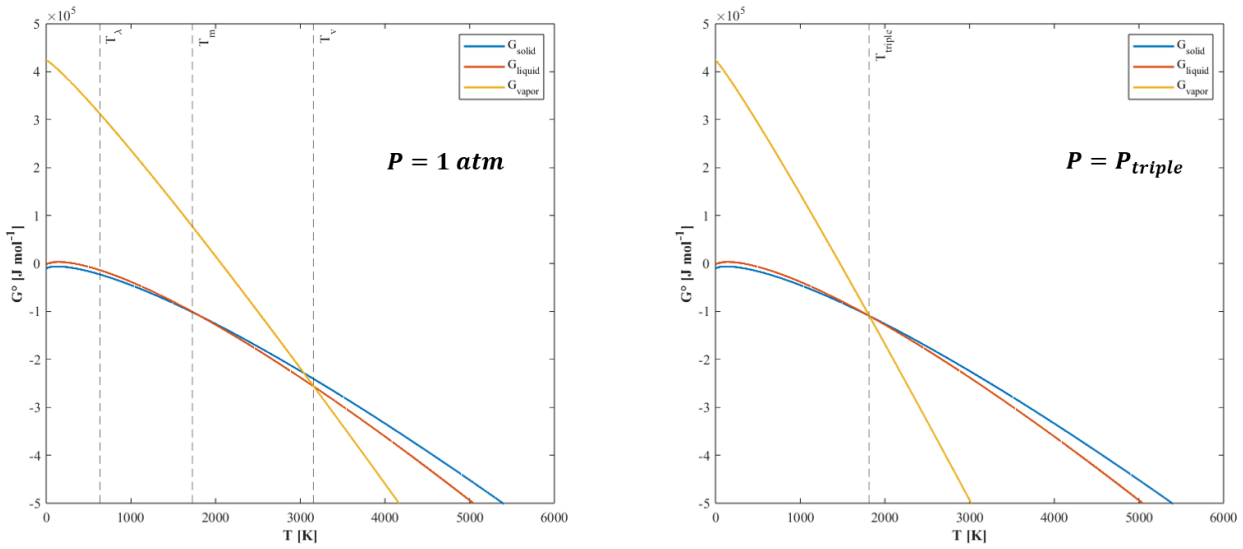

Figure 9. Gibbs free energy of solid, liquid, and gas phases at standard state (left) and triple point pressure (right), Ni

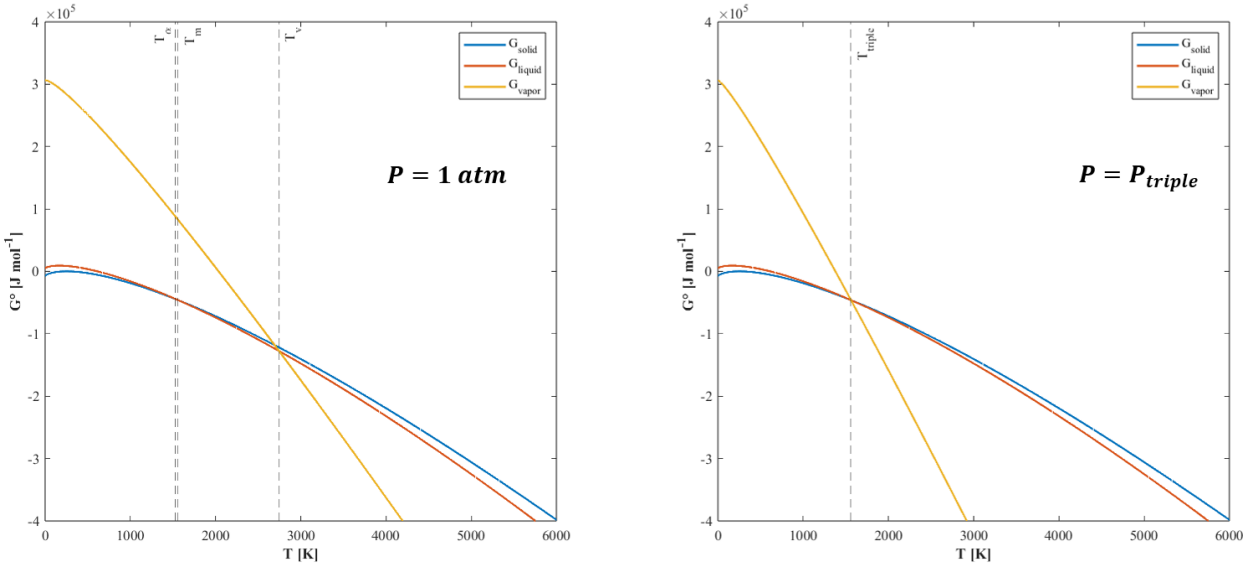

Figure 10. Gibbs free energy of solid, liquid, and gas phases at standard state (left) and triple point pressure (right), Be

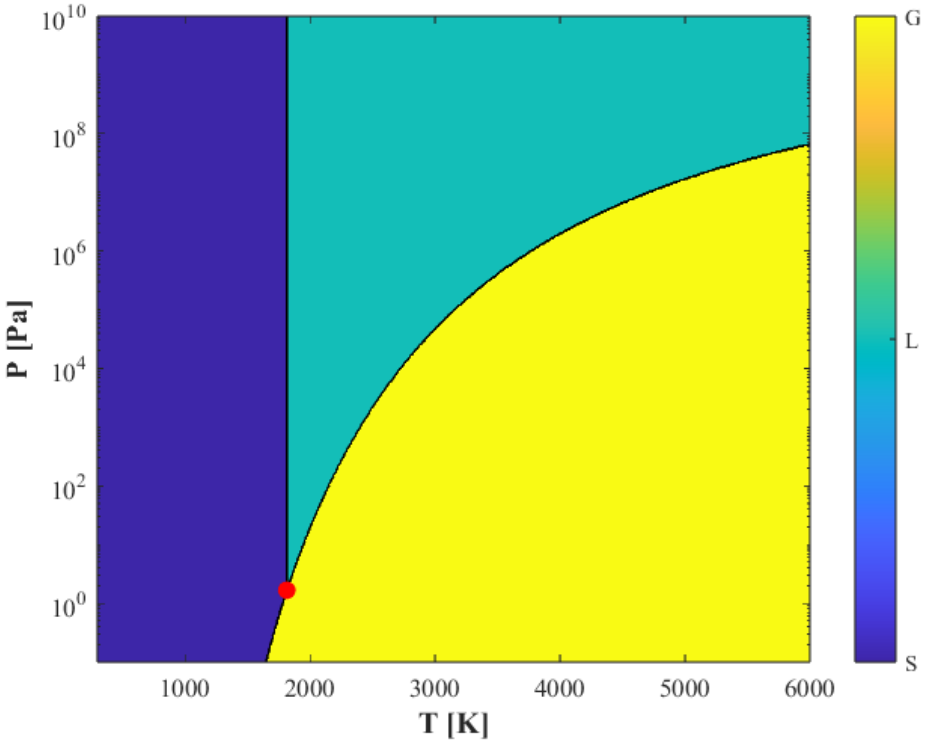

Figure 11. Field-Field Phase Diagram, Ni

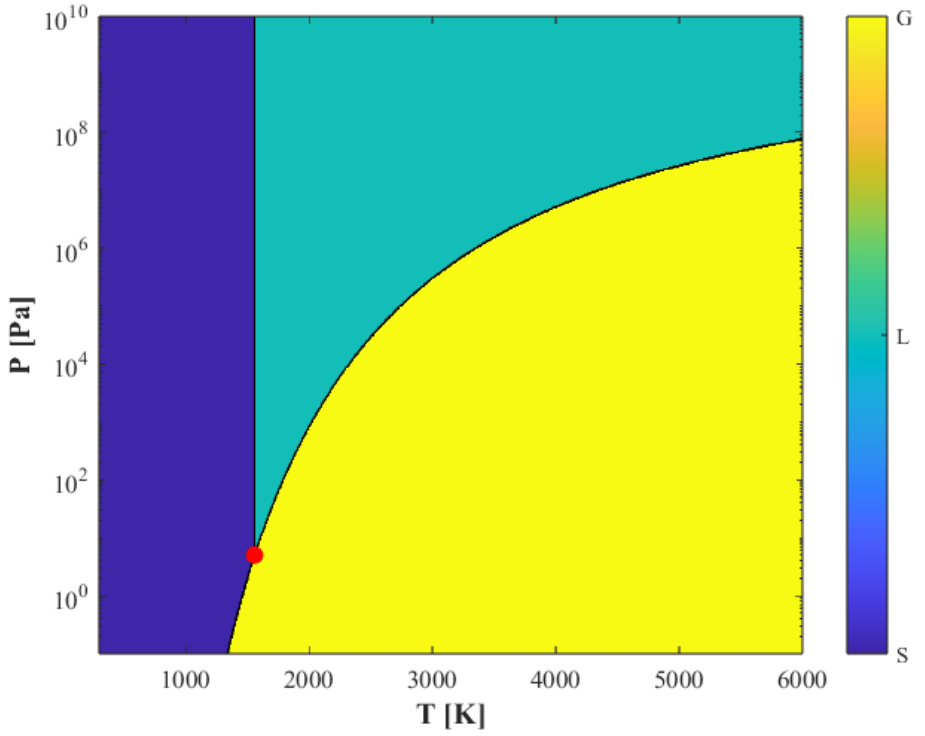

Figure 12. Field-Field Phase Diagram, Be

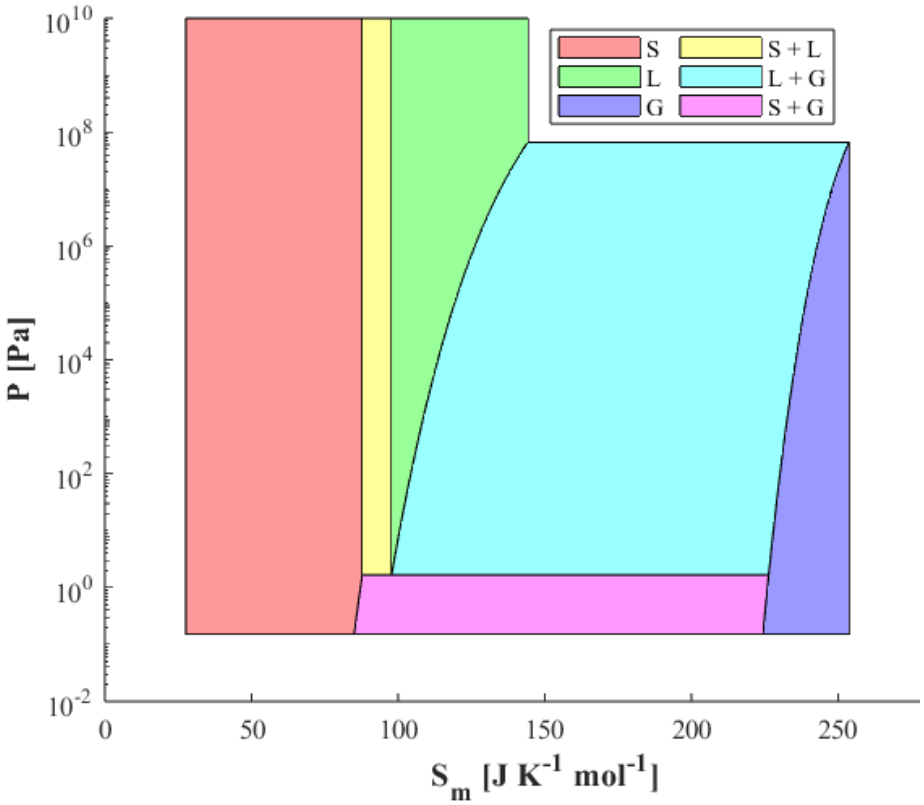

Figure 13. Field-Density Phase Diagram, Ni

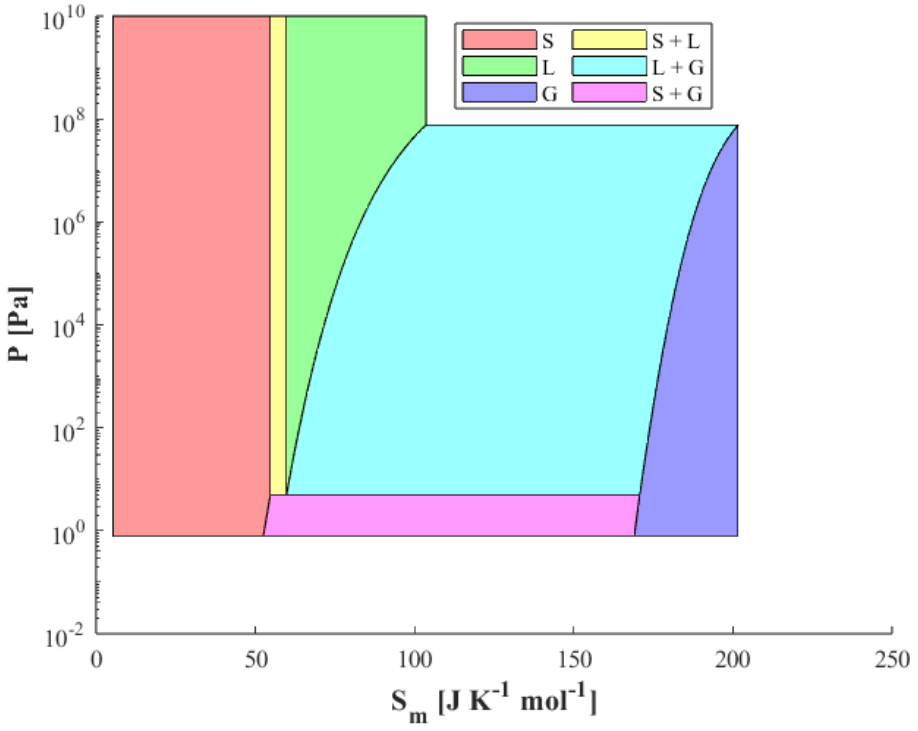

Figure 14. Field-Density Phase Diagram, Be

Figure 15 illustrates the Be-Ni phase diagram calculated using the Be-Ni thermodynamic database generated by this study. This phase diagram is a graphical representation of the thermodynamic models calculated by ESPEI using the phase model and experimental thermodynamic data detailed in Section 2.5. Zero-point function experimental data published in Okamoto and Tanner's study [1] is superimposed on the calculated phase diagram for reference.

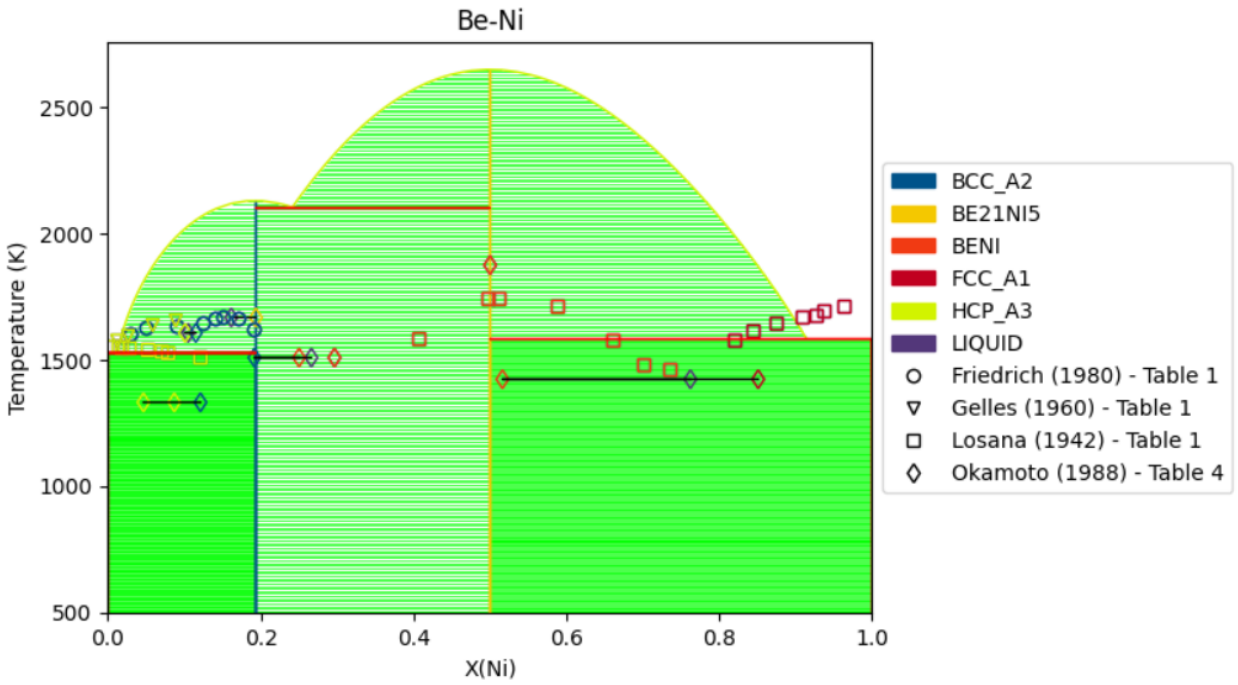

Figure 15. Calculated Be-Ni Phase Diagram

4. Discussion

The following discussion focuses on analyzing the Be-Ni phase diagram calculated by this study in comparison to Okamoto and Tanner's authoritative assessment of the Be-Ni system [1]. Analysis of results related to the investigation of the pure elements will not be emphasized in this report as the author has discussed these results in prior studies, which are publicly available through the author's GitHub repository for this study [12].

Figure 16 illustrates the Be-Ni phase diagram calculated by Okamoto and Tanner, originally published in 1988 [1]. As recently as 2016, Okamoto and Tanner's study of the Be-Ni has been

referenced as the authoritative source on the system, indicated by their inclusion in the ASM Handbook of Alloy Phase Diagrams [13].

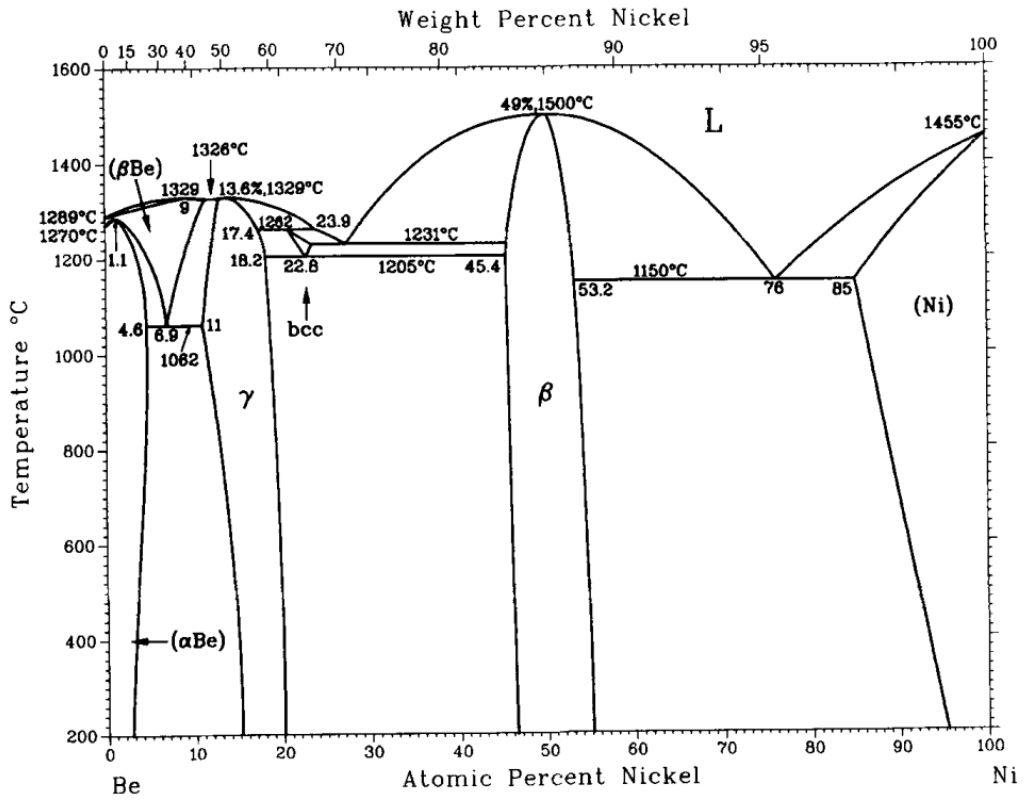

Figure 16. Be-Ni Phase Diagram, Okamoto and Tanner, 1988 [1].

There are few similarities and clear discrepancies between Figure 15, the Be-Ni phase diagram calculated by this study, and Figure 16, the reference Be-Ni phase diagram, despite this study using the same experimental data. Beginning with the similarities, the phase diagram calculated by this study does depict a general topology that is similar to Figure 16. Most evidently, the liquidus line features two quadratic curves, one from 1.20 at% Ni to 24.13 at% Ni and a second from 24.13 at% Ni to 91.42 at% Ni, which matches the topology of Figure 16. Important discrepancies that can be observed when considering these two liquidus curves are the temperature range they span and their terminal compositions. In Figure 15, the liquidus line exists from 1527 K to a maximum exceeding 2500 K, whereas the liquidus line in Figure 16 exists from 1562 K to 1773 K. This suggests that the liquidus line near the pure elements is accurate, but the

curvature defining the liquidus line at intermediate compositions is scaled incorrectly. This is supported by the experimental data points at low at% compositions of Ni plotted on the calculated phase diagram, where the calculated liquidus line and experimental data points overlap.

Figure 15 fails to calculate a liquidus line for αBe and Ni; however, plotting the generated .tdb file in Pandat, Figure 17, does illustrate these missing liquidus curves. Why Pandat is able to plot these liquidus lines and the ESPEI library are unable to requires further investigation. The liquidus lines featured in Figure 17 resemble those featured in Figure 16 and the experimental data plotted in Figure 15. Figure 18 and Figure 19 zoom in on the αBe liquidus line and Ni liquidus line, respectively. In Figure 19, the discrepancy in terminal composition of the Ni liquidus line becomes more evident. Where Okamoto calculates a eutectic composition of 76 at% Ni for the $L \leftrightarrow \beta + \mathrm{Ni}$ reaction, this study's phase diagram calculates a eutectic composition of 91.42 at% Ni. Subsequently, the eutectic temperature calculated for this reaction by this study is higher than Okamoto's estimate (1582.6953 K versus 1423 K).

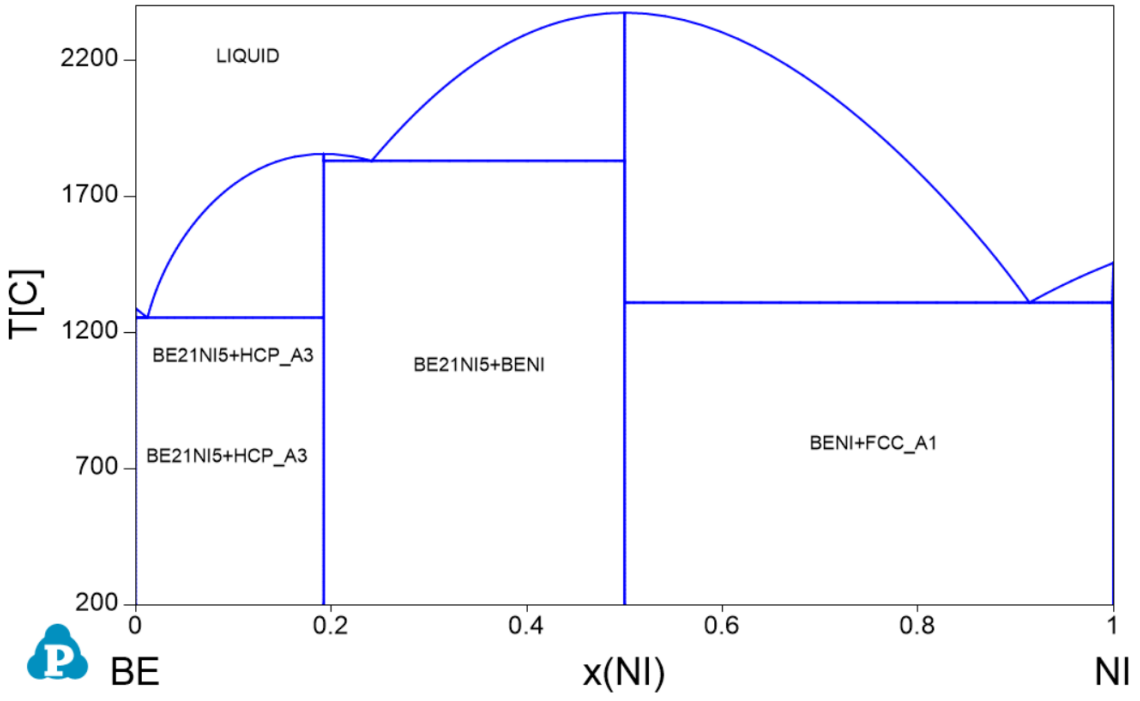

Figure 17. Calculated Be-Ni Phase Diagram, Pandat

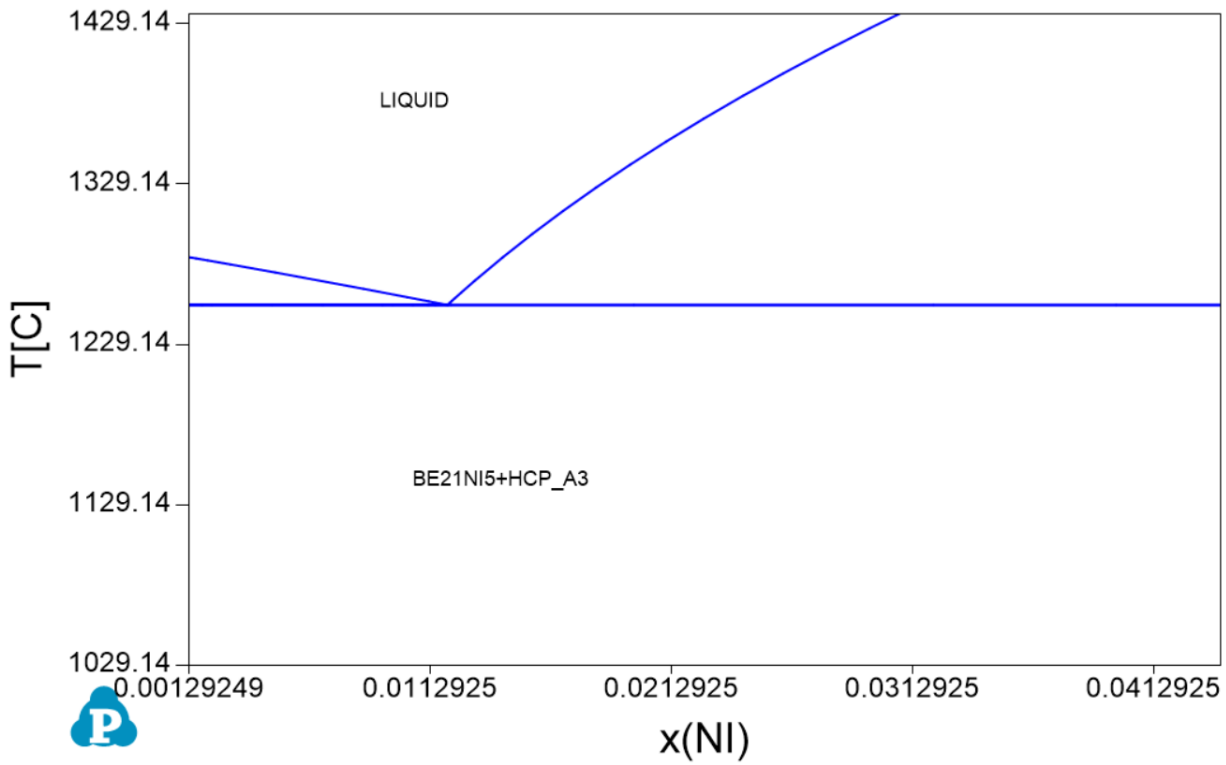

Figure 18. Calculated Be-Ni Phase Diagram, αBe Liquidus Line, Pandat

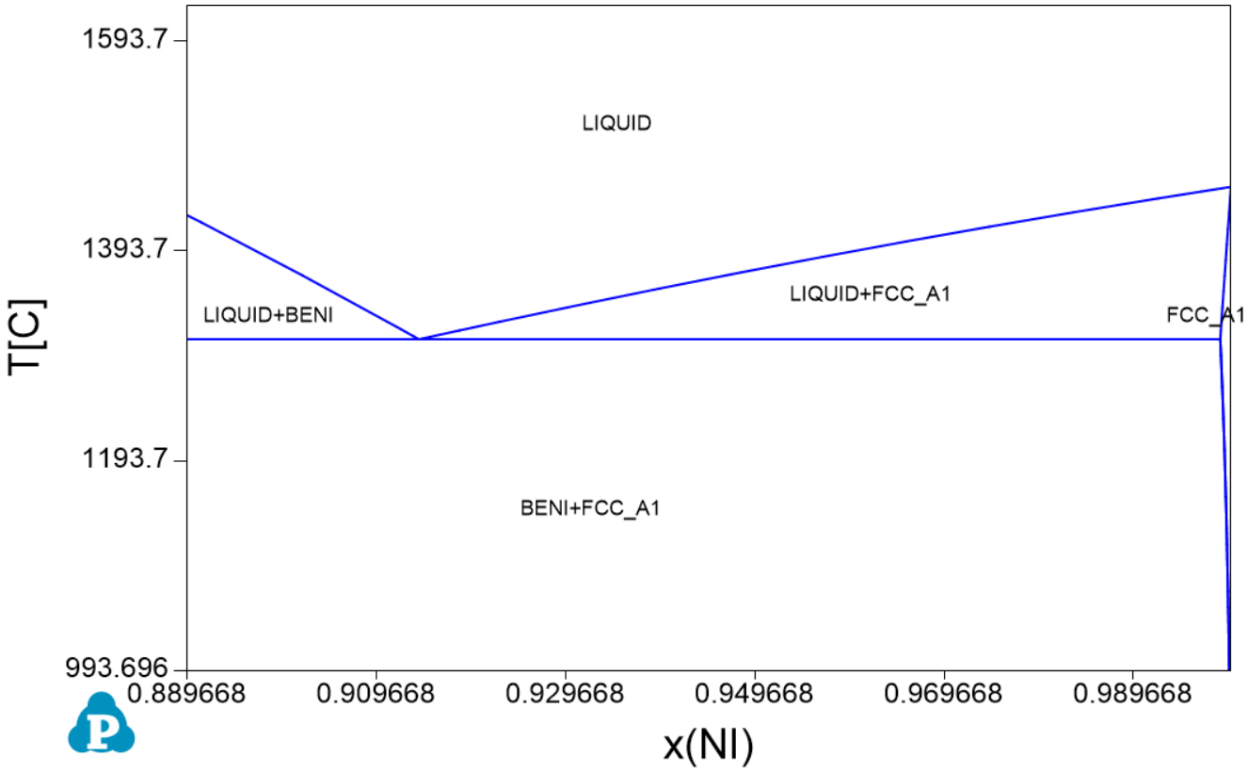

Figure 19. Calculated Be-Ni Phase Diagram, Ni Liquidus Line, Pandat

Using Figure 17 and Pandat's "Table" feature, the calculated phase transition temperature of Ni and Be can be assessed along with the temperatures associated with the system's invariant reactions. Table 7 and Table 8 report these temperatures, comparing this study, Okamoto's estimates, and NIST-JANAF reference data. The phase transition temperatures for pure Ni and Be reflected in Figure 17 agree with reference data. The liquid-to-vapor transition temperature was not calculated by this study or estimated by Okamoto as this phase is beyond the temperature range of interest for most applications.

Table 8 highlights the stark discrepancy between the phase diagram calculated by this study and the phase diagram calculated by Okamoto. Of the four invariant reactions estimated by Okamoto, only one (reaction 6, Table 8) is featured in this study's phase diagram. Reaction 1 (eutectoid), reaction 3 (eutectic), and reaction 4 (peritectic) are not featured in this study's phase diagram, but similar reactions are. For example, instead of Okamoto's eutectic reaction $L \leftrightarrow (\beta\mathrm{Be}) + \gamma$, this study's phase diagram features $L \leftrightarrow (\alpha\mathrm{Be}) + \gamma$. Similarly, instead of $L + \gamma \leftrightarrow \beta$, this study features $L \leftrightarrow \gamma + \beta$. Unsurprisingly, these substitute reactions occur a different temperatures and compositions when compared to Okamoto's reactions, but the structure of the error (forming αBe instead of βBe and γ being included on the wrong side of the reaction), indicates a likely source of error that will now be discussed.

Table 7. Comparison of calculated phase transition temperatures [K]

	Bali	**Okamoto and Tanner [1]**	**NIST–JANAF [3, 4]**
Nickel			
T_m	1728.0850	1728	1728
T_v	-	-	3156.584
Beryllium			
T_α	1527.0012	1543	1527
T_m	1559.9899	1562	1560
T_v	-	-	2741.437

Table 8. Comparison of calculated invariant reactions temperatures [K]

		Bali		Okamoto and Tanner [1]	
No.	**Reaction**	**T [K]**	**C [at% Ni]**	**T [K]**	**C [at% Ni]**
(1)	$(\beta\mathrm{Be}) \leftrightarrow (\alpha\mathrm{Be}) + \gamma$	-	-	1335	6.9%
(2)	$L \leftrightarrow (\alpha\mathrm{Be}) + \gamma$	1527.0012	1.20%	-	-
(3)	$L \leftrightarrow (\beta\mathrm{Be}) + \gamma$	-	-	1599	13.6%
(4)	$L + \gamma \leftrightarrow \beta$	-	-	1504	~28%
(5)	$L \leftrightarrow \gamma + \beta$	2102.9561	24.13%	-	-
(6)	$L \leftrightarrow \beta + \mathrm{Ni}$	1582.6953	91.42%	1423	76%

One dramatic discrepancy between this study's phase diagram and Okamoto's, which is hypothesized to be a principal contributor to the poorly estimated invariant reactions, is the lack of γ ($Be_{21}Ni_5$) and β (BeNi) phase fields. This is to say that the γ and β are being treated at intermetallic compounds with strict stoichiometric ratios, rather than solution phases that have solubility ranges. This was a consequence of inconsistencies, caught after the fact, between how these phases were defined in the phase model .json file and how experimental enthalpy of formation data was formatted into .json files for these phases. Based on the phase model, sublattice mixing was possible as vacancies were included in the sublattice structure of each phase. However, the vacancy sublattice was neglected when formatting the experimental data, resulting in ESPEI interpreting the data to be associated with a fixed sublattice structure, where no mixing was allowed. Therefore, each phase was treated as an intermetallic compound with fixed stoichiometric ratios as that is what the input data reflected.

A likely path forward to correct the curvature of the liquidus lines (temperature range of each liquidus line and terminal compositions) is to optimize the .tdb model parameters using MCMC optimization. This optimization routine fits phase boundaries to zero-point function data, such as temperature of the liquidus, solidus, or solvus line at different compositions, resulting in phase diagrams that are more representative of experimental data points.

5. Conclusion

This study investigated the Be-Ni system and attempted to generate a thermodynamic database for the binary system. The study evaluated fundamental thermodynamic properties of each pure element, resulting in calculations of the element's unary phase diagram. Lastly, the binary thermodynamic database was calculated using ESPEI, leading to the following conclusions:

- The study successfully produced an initial estimate of the Be-Ni thermodynamic database (.tdb) file using crystal structure, enthalpy of mixing, and enthalpy of formation experimental data.
- The initial .tdb fit accurately estimated the phase transition temperature of the two components making up the system and the topology of the liquidus curves.
- The initial .tdb fit failed to accurately predict established invariant reactions for the Be-Ni system due to inadequate modeling of solution phases that exist within the system.
- With limited enthalpy of mixing and enthalpy of formation experimental data, MCMC optimization using zero-point function data is recommended to tune model parameters to match experimental results.

Acknowledgements

The author wishes to thank Professor Eric Payton of the University of Cincinnati and fellow MTEN 6005 students for their guidance, technical assistance, and support throughout the project. The author would also like to acknowledge the use of Claude Sonnet 4.5 as a programming resource used throughout the project. Claude Sonnet 4.5 was primarily used as a MATLAB de-bugging tool, but also assisted as a Fortran "translator" to encode experimental thermodynamic data into .json files for use with the ESPEI Python library.

References

[1] H. Okamoto and L. E. Tanner, “The Be-Ni (Beryllium-Nickel) System,” *Bulletin of Alloy Phase Diagrams*, vol. 9, no. 5, pp. 563–573, 1988.

[2] B. Hallstedt, “The SGTE collection of binary datasets,” *Calphad*, vol. 89, p. 102833, Jun. 2025, doi: https://doi.org/10.1016/j.calphad.2025.102833.

[3] *Nist.gov*, 2025. https://janaf.nist.gov/tables/Ni-001.html

[4] *Nist.gov*, 2025. https://janaf.nist.gov/tables/Be-001.html

[5] “Create Fit Types for Library Models,” *Mathworks.com*, 2021. https://www.mathworks.com/help/curvefit/fittype.html

[6] “Fit curve or surface to data - MATLAB fit,” *www.mathworks.com*. https://www.mathworks.com/help/curvefit/fit.html

[7] Y. Austin Chang and W. Alan Oates, *Materials Thermodynamics*. John Wiley & Sons, 2010.

[8] “Find minimum of constrained nonlinear multivariable function - MATLAB fmincon,” *www.mathworks.com*. https://www.mathworks.com/help/optim/ug/fmincon.html

[9] “Phase Models Schema – ESPEI,” *Espei.org*, 2025. https://espei.org/reference/phase_models_schema.html (accessed Dec. 09, 2025).

[10] “ESPEI Dataset Schema – ESPEI,” *Espei.org*, 2019. https://espei.org/reference/dataset_schema.html (accessed Dec. 09, 2025).

[11] “Cu-Mg Example – ESPEI,” *Espei.org*, 2025. https://espei.org/tutorials/cu-mg-example/cu-mg-example.html (accessed Dec. 09, 2025).

[12] balianirudh, “GitHub - balianirudh/materials-thermodynamics-project: Fall 2025 MTEN 6005 materials thermodynamics project,” *GitHub*, 2025. https://github.com/balianirudh/materials-thermodynamics-project/tree/main (accessed Oct. 30, 2025).

[13] H. Okamoto, M.E. Schlesinger, and E.M. Mueller, Eds., *ASM Handbook Alloy Phase Diagrams*, vol. 3. Materials Park, OH: ASM International, 2016